PAPER

Check for updates

Porphyrin bridged SnO₂/active layer for efficient and stable inverted organic solar cells

Jifa Wu, [ID] [a] Lihua Meng,[a] Yumeng Li,[a] Xinkang Wang,[a] Feng Tang,[b] Yinchun Guo,[a] Ting Wang,[a] Yuang Fu,[c] Xinhui Lu,[c] Baobing Fan,[a] Junwu Chen [ID] [a] and Xiaobin Peng [ID] *[a]

Interface modification of the electron transport layers (ETLs) is crucial to simultaneously enhance the efficiency and stability of inverted organic solar cells. In this work, we design and synthesize a porphyrin derivative with oligo ethylene glycol side chains (TPP-OEG) as a multifunctional interfacial modifier of the SnO₂ ETL. TPP-OEG effectively passivates the surface defects on SnO₂ and lowers its work function. Meanwhile, the oligo ethylene glycol side chains improve the interfacial compatibility with the active layer and regulate the film formation kinetics, improving molecular crystallization and interfacial ordering. Through this dual role, TPP-OEG acts as a molecular bridge that electronically and structurally couples SnO₂ with the active layer, enabling more balanced charge extraction, reduced recombination, and improved crystalline ordering. As a result, the inverted devices with TPP-OEG-modified SnO₂ ETLs achieve a champion power conversion efficiency of 19.60% based on the PM6:L8-BO:BTP-eC9 system, representing the highest reported efficiency for single-junction inverted OSCs to date. Moreover, the TPP-OEG devices show remarkably improved thermal and storage stability compared with the devices employing bare SnO₂ or TPP-modified SnO₂ ETLs. This study demonstrates that porphyrins with suitable tailored side chains offer a promising strategy for interface engineering in high-performance and stable organic photovoltaics.

Broader context

As one of the new renewable energy sources, organic solar cells (OSCs) have received a lot of attention from researchers due to their light-weight, low-cost and flexible-processing advantages. Despite recent increases in power conversion efficiency, intrinsic instability and interfacial losses remain major barriers to practical deployment. One critical challenge is engineering the electron transport layer (ETL) to facilitate efficient charge extraction and stable operation. In this work, we introduce a tailored porphyrin modifier with oligo ethylene glycol side chains (TPP-OEG) to optimize SnO₂ ETLs in inverted OSCs. The SnO₂/TPP-OEG based device achieves record efficiencies and enhanced stability compared to the control device, which provides an effective and feasible strategy for future interfacial studies.

Introduction

In recent years, single-junction organic solar cells (OSCs) have achieved power conversion efficiencies (PCEs) up to 21%, driven mainly by the development of novel non-fullerene acceptors and the optimization of active layer morphology.[1-5] However, most of these high-PCE devices employ the conventional device architecture using PEDOT:PSS. The acidic and hygroscopic nature of PEDOT:PSS can lead to electrode corrosion and active layer degradation, undermining device operational stability. Recently, most of these high-PCE devices have employed the conventional device architecture using self-assembled monolayers (SAMs) as the hole transport layer.[6] Despite their effectiveness in replacing PEDOT:PSS, SAMs can suffer from degradation and partial desorption under thermal or light stress, which may exacerbate leakage currents and enhance non-radiative recombination.[7-9] In addition, the simplified molecular structure and low molecular weight of SAM molecules confer reduced resistance to external stimuli such as heat and light, particularly under operational conditions.[10-12] In contrast, inverted architectures often provide enhanced stability, although their PCEs have typically lagged behind those of conventional devices.[13-16]

In inverted OSCs, commonly used electron transport layers (ETLs) such as zinc oxide (ZnO) or titanium oxide (TiO₂) are

[a]State Key Laboratory of Luminescent Materials and Devices, Institute of Polymer Optoelectronic Materials and Devices, Guangdong Basic Research Center of Excellence for Energy and Information Polymer Materials, South China University of Technology, 381 Wushan Road, Guangzhou, 510640, China

[b]International Collaborative Laboratory of 2D Materials for Optoelectronics Science and Technology of Ministry Education, Institute of Microscale Optoelectronics, Shenzhen University, Shenzhen 518060, P. R. China

[c]Department of Physics, The Chinese University of Hong Kong, New Territories, Hong Kong 999077, China. E-mail: chxbpeng@scut.edu.cn
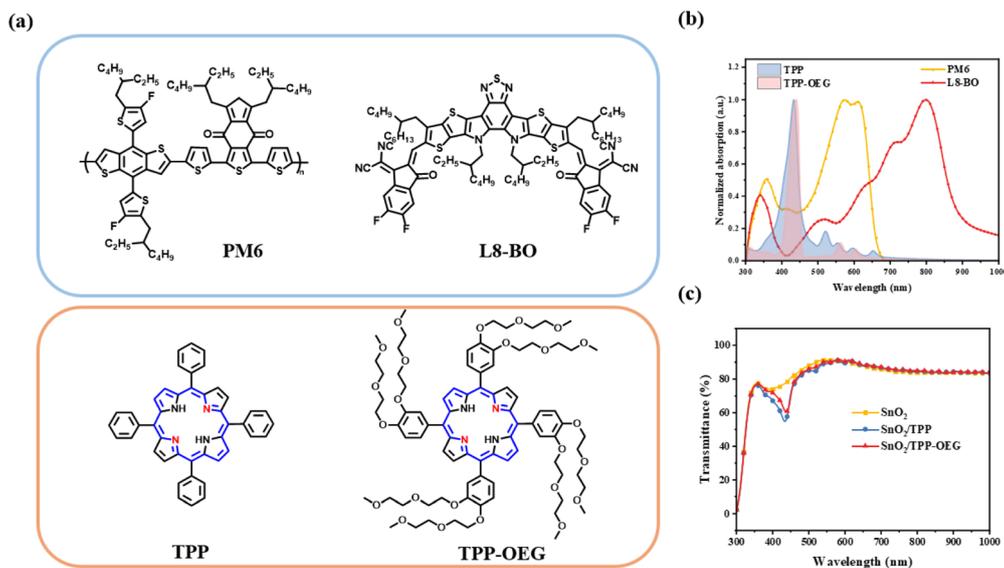
Fig. 1 (a) The chemical structures of PM6, L8-BO, TPP and TPP-OEG. (b) Absorption spectra of TPP, TPP-OEG, PM6 and L8-BO. (c) Optical transmittance spectra of SnO$_2$, SnO$_2$/TPP, and SnO$_2$/TPP-OEG films.

attractive due to their high optical transparency, solution processability, and good conductivity.[17,18] Nevertheless, ZnO and TiO$_2$ exhibit photocatalytic activity, which accelerates the degradation of the active layers and poses a challenge to long-term stability.[19,20] Compared with these ETLs, tin oxide (SnO$_2$) has emerged as a promising ETL for high performance inverted OSCs, owing to its lower photocatalytic activity, wider bandgap, excellent optical transmittance, and higher electron mobility.[21–24] Among various SnO$_2$ film fabrication methods, including spin-coating, drop-casting, blade coating, and atomic layer deposition (ALD), solution deposition using commercially available aqueous SnO$_2$ nanoparticle dispersions is especially attractive for scalable and cost-effective production.[25–27] However, such solution-processed SnO$_2$ films typically suffer from various surface defects (*e.g.*, oxygen vacancies and uncoordinated Sn sites).[28,29] These defects not only act as charge-carrier recombination centers, causing interfacial voltage losses, but also may trigger photochemical degradation of the active layer, limiting the device performance and operational lifetime.[30,31]

Interface engineering is effective for tuning and optimizing the properties of SnO$_2$ ETLs.[32] By introducing a suitable modification layer on the SnO$_2$ surface, the key interfacial parameters such as work function, surface energy, defect-state density, and chemical stability can be finely adjusted to improve the charge extraction and suppress the charge recombination. Conventional modification strategies include the use of conjugated electrolytes (*e.g.*, PFN),[33] organic salts (*e.g.*, PAS),[34] and functional small molecules,[35] which typically passivate surface defects and improve the energy level alignment through physical adsorption or chemical interactions.

Porphyrins, with large π-conjugated planar structures and abundant structural modification sites at the *meso* and β positions, have been widely applied in optoelectronic applications

due to their tunable chemical structures, distinctive optoelectronic properties, and coordination capability with metal ions.[36–42] The central nitrogen-containing macrocycle of free base porphyrins exhibits strong coordination affinity with metal sites, providing a promising pathway to form interfacial interactions with metal-oxide ETLs such as SnO$_2$. In our previous work, we demonstrated that simple tetraphenyl-porphyrin (TPP) can serve as an effective surface modifier for SnO$_2$,[43] where the coordination between the porphyrin core and the metal sites of the SnO$_2$ surface effectively passivates surface defects, leading to improved device efficiency and stability.

In this work, to further optimize the interfaces between SnO$_2$ and the active layers, we attach flexible oligo ethylene glycol (OEG) side chains onto the peripheral phenyl groups of TPP to construct a novel functional porphyrin molecule referred to as TPP-OEG (Fig. 1). This molecular design implements a dual strategy. First, TPP-OEG coordinates strongly with surface metal sites on SnO$_2$, enabling effective and stable passivation of surface defects and favorable modulation of the electronic structure of the ETL. Second, the oligo ethylene glycol side chains with higher polarity than alkyl chains improve the physical contact and compatibility with the SnO$_2$ ETL and active layer simultaneously, regulating active layer film formation kinetics and enhancing molecular crystallization. Therefore, compared with commonly reported interfacial modifiers for metal oxide electron transport layers, TPP-OEG functions as a molecular bridge that links SnO$_2$ and the active layer both electronically and structurally, thereby enhancing the device performance and stability. As a result, the SnO$_2$/TPP-OEG devices using PM6 and L8-BO as the active materials achieve a PCE of 19.02%, significantly surpassing both the SnO$_2$ devices (16.68%) and the SnO$_2$/TPP devices (18.35%). Additionally, the SnO$_2$/TPP-OEG ternary device based on PM6:L8-BO:BTP-eC9 achieves a PCE of 19.60%, which is one of the highest PCEs

for inverted OSCs. Moreover, the SnO_2/TPP-OEG device demonstrates superior stability including under dark storage and thermal aging. This work, which combines coordination-based defect passivation with improved interfacial compatibility, introduces a promising new strategy for designing high performance materials for SnO_2 interface modification.

Results and discussion

The chemical structures of PM6, L8-BO, TPP, and the synthesized porphyrin derivative TPP-OEG are shown in Fig. 1a. The detailed synthesis procedures and characterization of TPP-OEG are provided in the SI. As shown in Fig. 1b, the absorption maximum of TPP-OEG is observed at 440 nm, and that of TPP is at 433 nm. Critically, these absorption bands show minimal overlap with the main absorption region of the active layer materials, ensuring that the active layer can still efficiently harvest incident photons. We further characterized the optical transmission properties of bare SnO_2, SnO_2/TPP, and SnO_2/TPP-OEG films. As shown in Fig. 1c, within the wavelength range of 360–580 nm, the transmission of the SnO_2 films coated with porphyrin materials is reduced owing to absorption by the porphyrins (Fig. 1c).

To understand their intermolecular interactions, we first computed the electrostatic potential (ESP) surface maps of TPP-OEG to illustrate the regions of positive and negative charges, which help to predict the possible electrostatic interactions between TPP-OEG and SnO_2. Fig. S5 and S6 show the electrostatic potential distribution for the TPP-OEG molecule and the average potential values of its atoms. For the TPP-OEG molecule, the aromatic nitrogen atoms in the porphyrin core that are not bonded to hydrogen exhibit the lowest electrostatic potential, with absolute values exceeding -25 kcal mol^{-1}, consistent with previously reported potential distributions for the TPP molecule.[43] In contrast to TPP, in TPP-OEG the electronegative

oxygen atoms in the introduced polar oligo ethylene glycol side chains also appear as regions of strong negative potential (red regions). The deeper negative potential regions indicate higher electron density and a stronger ability to attract positive charge. Accordingly, when TPP-OEG is used to modify the SnO_2 surface, stronger electrostatic interactions are expected between the negatively charged regions on TPP-OEG (O and N atoms) and electron-deficient or positively charged sites on the SnO_2 surface.

Then, we performed quantum chemical calculations to gain deeper insight into the interaction dynamics between TPP-OEG and SnO_2. All calculations were carried out using the ORCA 5.0.4 software package and the electronic structure was described using the B3LYP density functional.[44] A nonperiodic rutile-type tetragonal SnO_2 ($P4_2/mnm$) cluster model containing 33 atoms (Fig. 2a) was constructed for the calculations because rutile-type tetragonal SnO_2 is the most thermally and chemically stable crystal structure under ambient conditions.[45,46] The independent gradient model based on Hirshfeld partitioning (IGMH) was employed to qualitatively analyze the noncovalent interactions within the interfacial complexes, enabling clear identification of coordination interactions, van der Waals forces, and steric effects at the interface.[47] Detailed parameters are provided in the SI. The optimized adsorption configurations of TPP and TPP-OEG on the SnO_2 surface are shown in Fig. 2a and b, respectively. In both cases, the porphyrin molecules interact with the SnO_2 substrate primarily through the coordination between the nitrogen atoms in the porphyrin core and the surface Sn atoms. In addition, the introduction of oligo ethylene glycol side chains in TPP-OEG provides additional electronegative oxygen atoms that further interact with the SnO_2 surface. As a result, the net electron transfer of approximately 1.17 e from SnO_2 to TPP and 1.21 e to TPP-OEG and the calculated binding energy of SnO_2/TPP-OEG is -9.693 eV, which is substantially larger than that of SnO_2/TPP(-7.744 eV). This
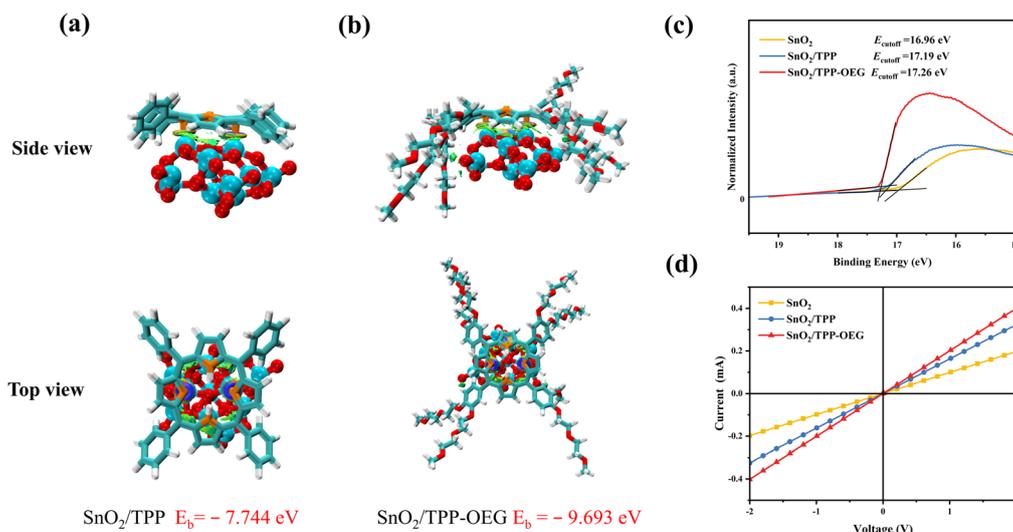

Fig. 2 The optimized geometry model of (a) SnO_2/TPP and (b) SnO_2/TPP-OEG. (c) Ultraviolet photoelectron spectroscopy (UPS) spectra and (d) I–V curves of SnO_2, SnO_2/TPP, and SnO_2/TPP-OEG films.
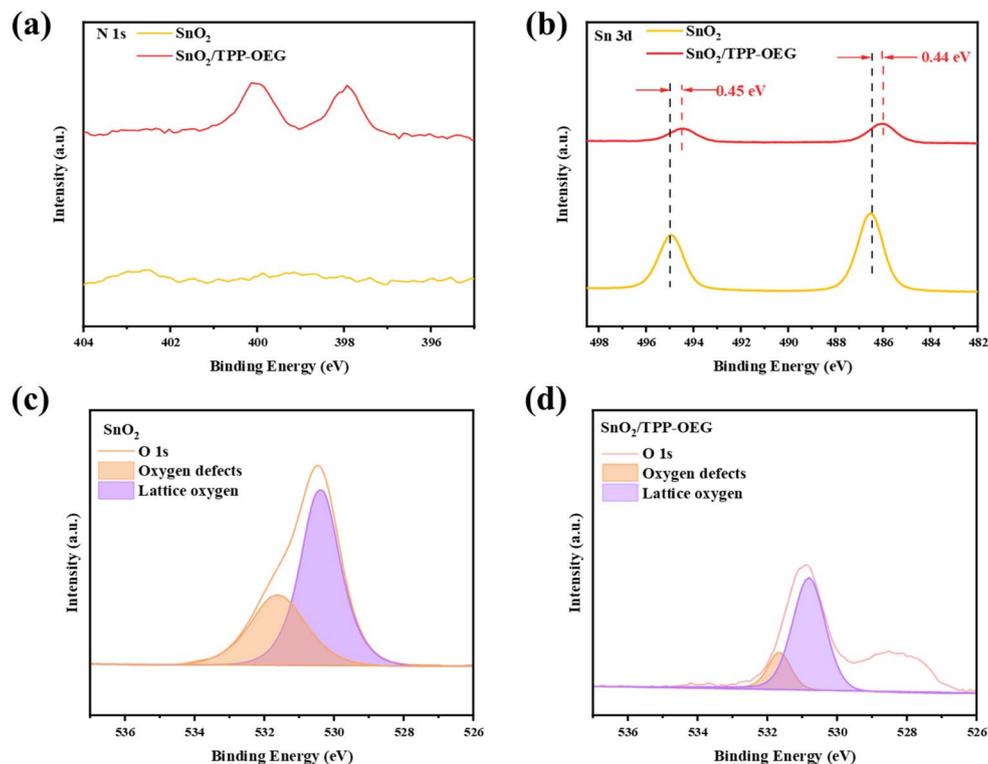
Fig. 3 (a) N 1s core level spectra, (b) Sn 3d core level spectra and (c and d) O 1s core level spectra of the SnO_2 and SnO_2/TPP-OEG films.

enhanced noncovalent interaction strength is consistent with the trends observed in XPS measurements, as reported below.

Interfacial charge redistribution of the porphyrins and SnO_2 was further examined by charge density difference ($\Delta\rho$) analysis, as shown in Fig. S7. A clear increase in the electron density is observed on the SnO_2 surface, accompanied by reduction in the electron density on both TPP and TPP-OEG molecules. Notably, pronounced charge transfer is also evident from the oligo ethylene glycol side chains of TPP-OEG toward SnO_2, further confirming the strong interfacial noncovalent interactions between TPP-OEG and SnO_2. Such strengthened interfacial charge transfer is expected to improve the interfacial dipole, thereby modulating the electronic structure of the electron transport layer and improving interfacial properties.

To further validate the quantum chemical calculations results, ultraviolet photo-electron spectroscopy (UPS) measurements were carried out to determine the secondary electron cutoff edges and the corresponding work functions of SnO_2, SnO_2/TPP, and SnO_2/TPP-OEG films (Fig. 2c).[48] The E_{cutoff} values are 16.96, 17.19 and 17.26 eV, corresponding to the work functions of 4.26, 4.03 and 3.96 eV, respectively. Due to the quasi-symmetric structure of TPP-OEG, its intrinsic molecular dipole is extremely small. Therefore, the reduction of the work function of SnO_2 after the porphyrin modification indicates the formation of an interfacial dipole, which effectively lowers the energy barrier for electron transfer at the ETL/active layer interface to facilitate electron extraction, suppresses interfacial charge recombination and improves the device performance.

In addition, the electrical conductivity of the ETLs was evaluated using a device structure of ITO/ETL/Ag. As shown in Fig. 2d, both TPP and TPP-OEG modified SnO_2 films exhibit higher conductivity than bare SnO_2, and SnO_2/TPP-OEG exhibits the highest conductivity, suggesting that porphyrin modification effectively improves the interfacial contact, and facilitates the ohmic contact. Furthermore, the incorporation of oligo ethylene glycol side chains can further reduce the work function of SnO_2, thereby enabling more efficient charge transport.

To further confirm the interactions between the porphyrin molecules and SnO_2 and to investigate the surface defects on SnO_2, we performed X-ray photoelectron spectroscopy (XPS) on SnO_2, SnO_2/TPP and SnO_2/TPP-OEG films. As shown in Fig. S8 and S9, in both SnO_2/TPP and SnO_2/TPP-OEG films, we observe N 1s signals that are not present in the pristine SnO_2 film, confirming that the two porphyrins are adsorbed on the SnO_2 surface. As shown in Fig. 3a, for the SnO_2/TPP-OEG film, two distinct N 1s peaks are observed: a peak at approximately 400.0 eV corresponding to imine nitrogen and a peak at around 398.0 eV corresponding to pyrrolic nitrogen. Notably, pyrrolic nitrogen generally participates more strongly in interfacial interactions.[49–51]

Fig. 3b and S9c show the Sn 3d core level spectra of the different ETL films. The peak positions and shapes are very similar across the three samples, indicating that neither TPP nor TPP-OEG modification substantially alters the crystalline structure of SnO_2. However, the both porphyrin modified SnO_2 films show shifts of the Sn 3d peaks toward lower binding
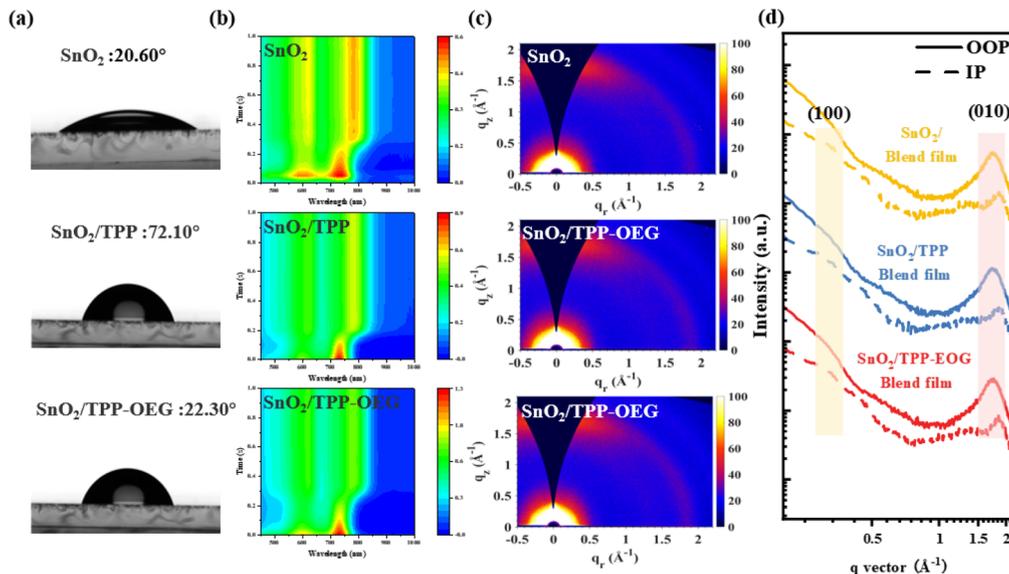
Fig. 4 (a) Water contact angles of SnO$_2$, SnO$_2$/TPP and SnO$_2$/TPP-OEG. (b) Time-resolved UV-vis absorption spectra and (c) grazing incidence wide-angle X-ray scattering patterns of PM6:L8-BO coated upon SnO$_2$, SnO$_2$/TPP and SnO$_2$/TPP-OEG films. (d) Out-of-plane (OOP) line cuts and in-plane (IP) line cuts of the GIWAXS patterns.

energy, indicating an increased electron density around the tin atoms induced by the interactions with the porphyrin molecules. Notably, the binding energy shift for SnO$_2$/TPP-OEG is slightly larger, in the range of approximately 0.44–0.45 eV, compared with about 0.40 eV for SnO$_2$/TPP, suggesting that the introduction of the polar oligo ethylene glycol side chains further is beneficial for the formation of an interfacial dipole and charge transfer at the interfaces.

To further analyze the oxygen vacancy defects, we examined the O 1s core level spectra of the three films (Fig. 3c–d and S9d). During the thermal annealing of solution-processed SnO$_2$ films under ambient conditions, surface hydroxylation naturally occurs, leading to several kinds of hydroxyl groups on the SnO$_2$ surface: (1) basic hydroxyls binding to Sn sites and (2) acidic bridging hydroxyls binding to metal sites, as well as oxygen vacancies and uncoordinated Sn sites that can adsorb environmental O$_2$/H$_2$O.[23] These defects can trap electrons and form barriers to electron transport, which strongly undermine charge extraction, photovoltaic performance, and device stability. The O atoms of SnO$_2$ can be divided into two classes, one is the lattice oxygens (low binding energy peak) of O–Sn bonding, and the other is the defective oxygens (high binding energy peak) with surface hydroxyl groups. For the bare SnO$_2$ film, the ratio of defective oxygens to lattice oxygens is approximately 0.43 in terms of peak height and about 0.53 in terms of integrated area. After modification with TPP and TPP-OEG, the defective oxygen to lattice oxygen height ratios decrease to around 0.35 and 0.32, respectively. The defective oxygen to lattice oxygen area ratios also decrease from 0.53 for bare SnO$_2$ to about 0.40 for SnO$_2$/TPP and 0.36 for SnO$_2$/TPP-OEG. Notably, the high binding energy O 1s peak of SnO$_2$/TPP-OEG also includes contributions from the ether and hydroxyl oxygens of the OEG side chains (centered at 531.55 eV, Fig. S10), yet the relative intensity

compared to lattice oxygen remains lower than that in bare SnO$_2$. These results indicate that the modification of SnO$_2$ by both free porphyrins can reduce the density of oxygen vacancy defects, and that TPP-OEG is more effective in suppressing these defects. It should be noted that for SnO$_2$/TPP-OEG films, due to the introduction of oligoethylene glycol side chains, a significant O 1s signal appears in the lower binding energy region.

Beyond surface defect passivation, the OEG side chains play an important role in improving the physical contact and compatibility between the ETL and the typically hydrophobic organic active layer. Furthermore, by optimizing the ETL substrate surface characteristics, the film-formation kinetics of the active layer can be tuned, which can lead to improved morphology and enhanced device performance.[52]

We performed contact angle measurements using water and ethylene glycol on SnO$_2$, SnO$_2$/TPP, and SnO$_2$/TPP-OEG substrates (Fig. 4a, S11 and Table S2). The water contact angles are 20.60°, 72.10°, and 22.30° for SnO$_2$, SnO$_2$/TPP, and SnO$_2$/TPP-OEG, respectively. While SnO$_2$/TPP exhibits a distinctly hydrophobic surface, SnO$_2$/TPP-OEG exhibits hydrophilic behavior similar to that of SnO$_2$ due to the introduction of polar oligo-ethylene glycol (OEG) functional groups. However, as seen in Table S2, surface energy analysis using the Owens–Wendt–Rabel–Kaelble (OWRK) method reveals that TPP-OEG modification significantly increases the dispersive component,[53] making the surface energy of SnO$_2$/TPP-OEG closer to that of the predominantly dispersive organic active layer materials (PM6 and BTP-eC9) and enhancing the interfacial compatibility. Consequently, TPP-OEG not only effectively passivates surface defects on SnO$_2$ but also facilitates uniform solution spreading, nucleation, and controlled crystallization

during active layer deposition, leading to improved film morphology and device performance.

Compared with TPP, TPP-OEG not only effectively passivates surface defects on SnO$_2$ but also provides improved interfacial compatibility with SnO$_2$. However, because there are many polar groups in the active materials, the polar–polar interactions between the polar OEG groups of TPP-OEG and the active materials can also facilitate uniform solution spreading and nucleation during active layer deposition, which is critical for regulating the subsequent crystallization and morphology.

To directly probe these effects, we further studied the aggregation dynamics of the active layer during deposition on the three ETLs using time-resolved *in situ* absorption spectroscopy (Fig. 4b and S12). The film formation process can be divided into three stages: (I) solvent evaporation; (II) nucleation and crystal growth; and (III) the final dried film. As shown in Fig. 4b and S12d–f, during the initial stage I, the solvent continuously evaporates, and with increasing concentration the solution reaches its solubility limit, initiating nucleation. Under extreme supersaturation, the 0–0 peak of the L8-BO red-shifts continually, accompanied by a rapid change of the intensity, which reflects a liquid–solid phase transition from solution to a solid aggregation state and indicates the onset of L8-BO crystallization. For the active layer deposited on SnO$_2$/TPP and SnO$_2$/TPP-OEG, the initial onset of the L8-BO peak shift occurs slightly earlier than for bare SnO$_2$. This behavior can be attributed to the modified substrates possessing surface energy closer to that of the acceptor material, which promotes earlier crystallization. As solvent evaporation continues, the absorption peaks of BTP-eC9 and PM6 continue to redshift until the solvent is completely evaporated, and both the peak positions and intensities of the donor and acceptor are stabilized, indicating the formation of a structurally stable film in the final dried film stage. Notably, the crystal growth time during stage II is approximately 0.22 s for active layer films deposited on bare SnO$_2$, 0.18 s for SnO$_2$/TPP, and 0.30 s for SnO$_2$/TPP-OEG (Fig. S12d–f). These differences in crystal growth rates demonstrate that TPP and TPP-OEG induce different crystallization kinetics. In particular, the enhanced interfacial compatibility provided by the OEG side chains in TPP-OEG results in a slower and more moderated crystallization process. Such prolonged film formation kinetics are generally beneficial for achieving higher crystallinity, as they allow sufficient time for molecular diffusion, rearrangement, and ordering prior to solidification.

To further examine the impacts of the different ETLs on active layer morphology, grazing-incidence wide-angle X-ray scattering (GIWAXS) measurements were performed. Fig. 4c shows the 2D GIWAXS patterns of PM6:L8-BO blend films deposited on SnO$_2$, SnO$_2$/TPP, and SnO$_2$/TPP-OEG substrates, while Fig. 4d presents the corresponding in-plane (IP) and out-of-plane (OOP) line cuts, and the detailed fitting parameters are summarized in Table S1. All three active layer films exhibit face-on orientation, as evidenced by the strong π–π stacking diffraction peaks in the OOP direction and the (010) peak appears around 1.73 Å^{-1}. Specifically, the blend film deposited on bare SnO$_2$ shows a (010) peak at $q_z = 1.733$ Å^{-1}, corresponding to a *d*-spacing of 3.626 Å and a coherence length (CCL)

of 1.816 nm. For the SnO$_2$/TPP substrate, the (010) peak is located at $q_z = 1.734$ Å^{-1} with a *d*-spacing of 3.624 Å and a CCL of 1.877 nm. In contrast, the blend film on SnO$_2$/TPP-OEG exhibits its (010) diffraction peak at $q_z = 1.736$ Å^{-1}, with a *d*-spacing of 3.619 Å and a significantly larger coherence length of 1.982 nm. These results indicate that the film on SnO$_2$/TPP exhibits moderately enhanced face-on molecular orientation compared with the blend film on bare SnO$_2$, which can be attributed to surface energy modulation at the ETL by TPP to improve molecular crystallization and packing.[43] More importantly, the blend film deposited on SnO$_2$/TPP-OEG displays a further enhanced face-on orientation, as reflected by the further reduced intermolecular spacing and the further increased coherence length, indicative of tighter π–π stacking.

As shown in *in situ* absorption spectra, the extended crystallization time during the film formation enables sufficient molecular reorganization on SnO$_2$/TPP-OEG, which promotes more ordered packing of the acceptor molecules and facilitates efficient charge transport. In addition to enhancing charge transport, enhanced face-on orientation is also beneficial for morphological stability, since such domains typically contain fewer isolated amorphous regions that can act as traps and compromise long term device stability.[54]

We prepared the devices with the different ETLs to investigate the impacts of porphyrin modification on the photovoltaic performance of inverted organic solar cells (ITO/ETL/BHJ/MoO$_3$/Ag). All the devices employed a PM6 donor and L8-BO acceptor as the active layer materials, and the energy levels of the electrodes and interfacial work functions are illustrated in Fig. 5a. The *J–V* curves are shown in Fig. 5b and performance parameters are summarized in Table 1. The statistical distributions of key photovoltaic parameters based on 20 independent devices for each ETL configuration (violin plots) are shown in Fig. S13. The device based on bare SnO$_2$ as the ETL exhibited a power conversion efficiency (PCE) of 16.68% with a relatively low fill factor (FF) of 72.98%, indicating unbalanced charge transport within the device. The SnO$_2$/TPP-OEG device achieved a PCE of 19.02% with an open-circuit voltage (V_{OC}) of 0.881 V, a short-circuit current density (J_{SC}) of 26.97 mA cm^{-2}, and an FF of 80.03%, surpassing the SnO$_2$/TPP-modified device with a PCE of 18.35% ($V_{OC} = 0.877$ V, $J_{SC} = 26.53$ mA cm^{-2}, and FF = 78.86%). Among the three devices, the SnO$_2$/TPP-OEG device exhibits the best overall performance. This improvement can be attributed to the introduction of oligo ethylene glycol side chains, which enable TPP-OEG to function as a more effective interfacial bridge between SnO$_2$ and the active layer. In addition to defect passivation, TPP-OEG modulates interfacial compatibility and promotes favorable molecular crystallization and orientation within the active layer.

The external quantum efficiency (EQE) curves of the devices with and without porphyrin modification are shown in Fig. 5c. The integrated current densities calculated from the EQE spectra are 24.95, 25.36, and 25.80 mA cm^{-2} for the bare SnO$_2$, SnO$_2$/TPP, and SnO$_2$/TPP-OEG devices, respectively, which are consistent with the J_{SC} values obtained from the *J–V* curves. The porphyrin-modified devices exhibit enhanced EQE responses in the wavelength range from 550 to 900 nm. This improvement is
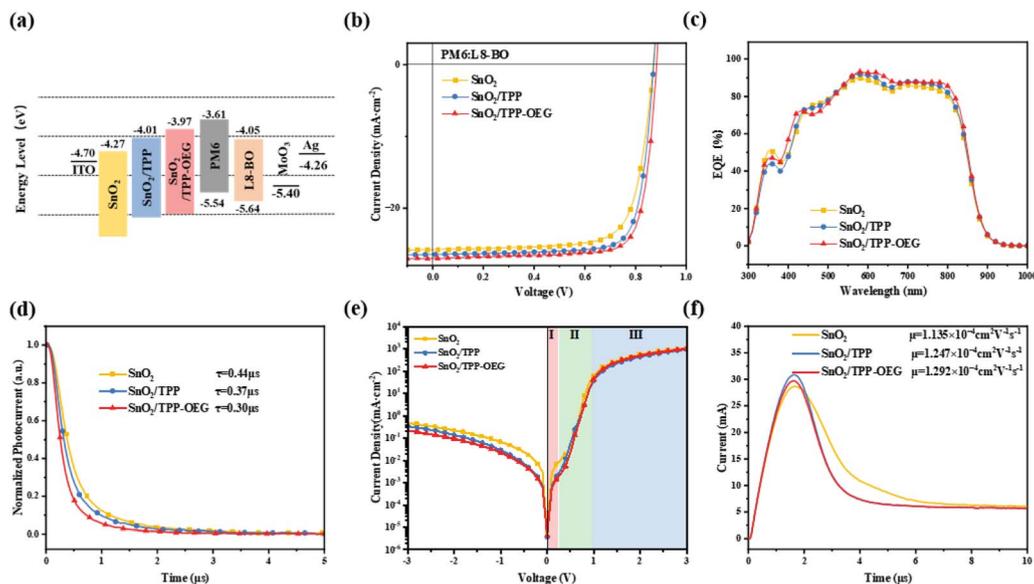
Fig. 5 (a) Schematic energy diagram of the materials in the PM6:L8-BO OSCs. (b) Current density–voltage (J–V) characteristics of the inverted OSCs under AM 1.5 G 1000 W m^{-2} irradiation. (c) EQE curves. (d) Normalized transient photocurrent traces. (e) Current–voltage curves of the devices based on different ETLs under dark conditions. (f) Photo-induced charge carrier extraction by linearly increasing voltage (photo-CELIV) curves.

attributed to suppressed non radiative recombination and enhanced charge collection efficiency. A slight reduction in EQE around 500 nm is observed for the porphyrin modified devices, which possibly originates from the subtle changes in optical interference conditions and interfacial morphology induced by the TPP-OEG interlayer. The introduction of TPP-OEG slightly modifies the optical thickness and dielectric environment at the SnO$_2$ active layer interface, which can lead to wavelength selective variations in the optical electric field distribution.[55]

To elucidate the origin of the improved photovoltaic performance, we first analyzed the reason for the increase in V_{OC} by the porphyrins. The built-in potential (V_{bi}) of a device sets an upper limit for the achievable V_{OC}. The V_{bi} was extracted from Mott–Schottky plots obtained from capacitance–voltage (C–V) measurements (Fig. S14). The V_{bi} of devices based on bare SnO$_2$, SnO$_2$/TPP, and SnO$_2$/TPP-OEG ETLs were determined to be 0.692, 0.719, and 0.745 V, respectively. The highest V_{bi} observed for the SnO$_2$/TPP-OEG device suggests that the SnO$_2$/TPP-OEG ETL has further improved the ohmic contact between the active layer and electrodes, facilitating more efficient electron extraction and contributing to an increase in V_{OC}.

To understand the enhanced J_{SC}, we investigated charge extraction, transport, and recombination dynamics. Transient

photocurrent (TPC) and transient photovoltage (TPV) measurements provide important insights into carrier dynamics in devices with the different ETLs. TPV measurements reflect carrier recombination behavior and carrier lifetime, where a slower carrier decay corresponds to a longer lifetime. As shown in Fig. S15, the SnO$_2$/TPP-OEG device exhibits a carrier lifetime of 26.44 µs, which is significantly longer than those of SnO$_2$ (18.48 µs) and SnO$_2$/TPP (21.50 µs). The prolonged carrier lifetime indicates suppressed recombination. TPC measurements quantify carrier extraction times. As shown in Fig. 5d, the charge extraction times for the SnO$_2$, SnO$_2$/TPP, and SnO$_2$/TPP-OEG devices are 0.44, 0.37, and 0.30 µs, respectively. Both porphyrin-modified devices exhibit substantially shorter extraction times than the bare SnO$_2$ device, indicating reduced charge transport barriers and more rapid extraction of photogenerated carriers from the active layer to the electrodes.

Charge transport and recombination behavior under dark conditions were further investigated by current–voltage (I–V) curves (Fig. 5e).[56] Under reverse bias, the SnO$_2$ TPP OEG device exhibits a markedly lower saturation current than the SnO$_2$ and SnO$_2$ TPP devices. In the zero bias and low forward bias regions, the SnO$_2$/TPP-OEG device also exhibits the lowest leakage current. These results indicate that porphyrin-based interface

Table 1 Device characteristics of the binary (PM6:L8-BO) OSCs based on different ETLs

ETL	V_{OC} [V]	J_{SC} [mA cm^{-2}]	J_{cal}[a] [mA cm^{-2}]	FF [%]	PCE[b] [%]
Bare SnO$_2$	0.872 (0.867 ± 0.004)	26.21 (25.84 ± 0.28)	24.95	72.98 (72.27 ± 0.46)	16.68 (16.23 ± 0.45)
SnO$_2$/TPP	0.877 (0.873 ± 0.003)	26.53 (26.24 ± 0.22)	25.36	78.86 (78.55 ± 0.24)	18.35 (18.04 ± 0.30)
SnO$_2$/TPP-OEG	0.881 (0.879 ± 0.002)	26.97 (26.82 ± 0.12)	25.80	80.03 (79.83 ± 0.15)	19.02 (18.78 ± 0.25)

[a] Calculated current density from the EQE curve. [b] he maximum PCE with the average values (in brackets) based on 20 devices.
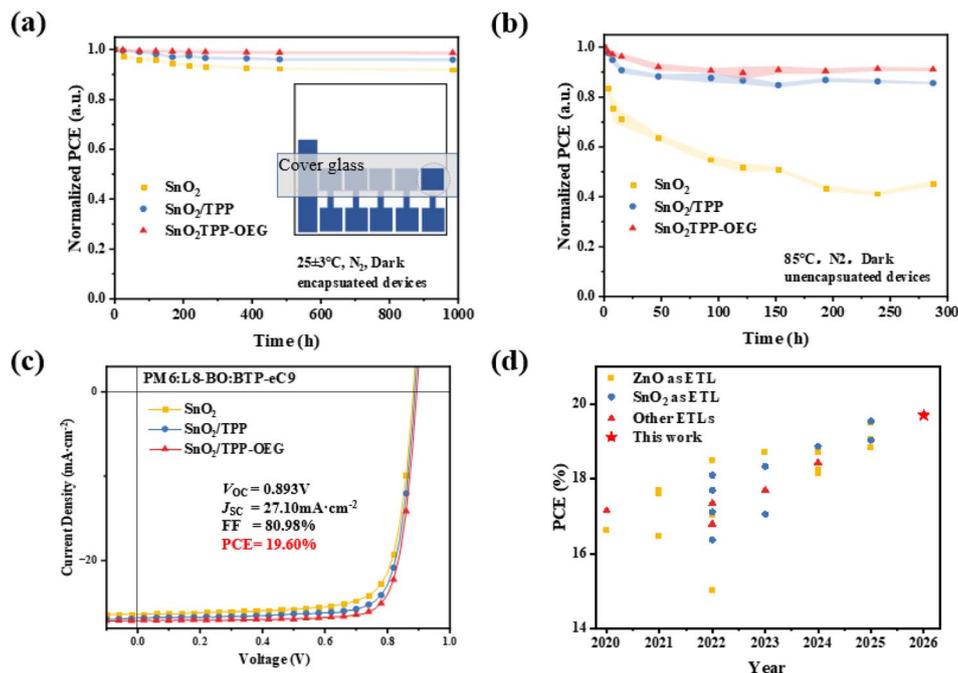
Fig. 6 (a) Storage stability and (b) thermal stability of the three devices. (c) J–V curves of the PM6: L8-BO:BTP-eC9 system based on the SnO$_2$/TPP-OEG device. (d) Comparison of our results with several representative PCEs of inverted OSCs reported previously.

modification effectively suppresses the interfacial charge recombination.

Electrochemical impedance spectroscopy measurements were performed to further probe the charge transport and recombination processes.[57] The Nyquist plots of the devices with the three different ETLs are shown in Fig. S16a, and the corresponding equivalent circuit model is presented in Fig. S16b. In this model, R_s represents the device series resistance, R_{BHJ} and C_{BHJ} correspond to the resistance and capacitance of the active layer, and R_{CTL} and C_{CTL} represent the resistance and capacitance of the charge transport layers, respectively. Fitting the Nyquist plots reveals that the SnO$_2$/TPP-OEG device has R_s, R_{BHJ}, and R_{CTL} values of 3.67, 80.43, and 63.94 Ω, respectively, which are significantly lower than those of the SnO$_2$/TPP device ($R_s = 7.44$ Ω, $R_{BHJ} = 93.86$ Ω, $R_{CTL} = 72.50$ Ω) and the bare SnO$_2$ device ($R_s = 21.97$ Ω, $R_{BHJ} = 146.23$ Ω, $R_{CTL} = 173.80$ Ω). The reduced resistances indicate that TPP-OEG provides more effective interface passivation that lowers oxygen vacancy defects on the SnO$_2$ surface and reduces charge transport resistance. In addition, the modification induces favorable morphological changes in the active layer to enhance charge transport and collection, consistent with the transient photocurrent and photovoltage measurements.

To further quantify trap states in the devices, capacitance–frequency (C–F) measurements were analyzed to extract the trap energy levels and trap densities (details of the calculation and measurement methods are provided in the SI). As shown in Fig. S17, the SnO$_2$/TPP-OEG device exhibits the lowest trap density in the shallow trap energy level range from 0.25 to 0.35 eV. This reduced density of shallow trap states facilitates carrier release prior to recombination. This reduction in trap

states contributes to an enhanced photocurrent response and is consistent with the EIS results. Taken together, these results indicate that the SnO$_2$/TPP-OEG device benefits from increased carrier lifetime, reduced trap density and charge recombination, and more efficient charge extraction, which collectively lead to the improved J_{SC}.

The FF of an organic solar cell is governed by the competition between the charge extraction and recombination, and it is influenced by many factors such as active layer thickness, morphology, recombination processes, and charge transport.[58] However, carrier mobility and recombination dynamics are generally the dominant parameters determining the FF. Since recombination dynamics have been discussed above, photo-induced charge carrier extraction by a linearly increasing voltage (photo-CELIV) and space-charge limited current (SCLC) were employed to further investigate the performance enhancements associated with the different ETLs.[59,60] Photo-CELIV results (Fig. 5f) reveal that the dynamic carrier mobility increases from 1.135×10^{-4} cm^2 V^{-1} s^{-1} for the bare SnO$_2$ device to 1.247×10^{-4} cm^2 V^{-1} s^{-1} for the SnO$_2$/TPP and 1.292×10^{-4} cm^2 V^{-1} s^{-1} for the SnO$_2$/TPP-OEG devices. The higher dynamic mobility observed for the SnO$_2$/TPP-OEG device suggests that charge extraction dominates over recombination, reflecting both suppressed recombination and enhanced extraction efficiency. Furthermore, SCLC measurements of the electron-only and the hole-only devices (Fig. S18) show that the electron mobilities (μ_e) for the devices based on SnO$_2$, SnO$_2$/TPP, and SnO$_2$/TPP-OEG are 1.75×10^{-4}, 1.93×10^{-4}, and 2.10×10^{-4} cm^2 V^{-1} s^{-1}, respectively, and the hole mobility (μ_h) of the hole-only device is 2.05×10^{-4} cm^2 V^{-1} s^{-1}. The resulting μ_h/μ_e ratios (Table S3) are 1.17, 1.06 and 0.98 for the SnO$_2$, SnO$_2$/

TPP, and SnO_2/TPP-OEG devices, respectively. The SnO_2/TPP-OEG device exhibits the highest and most balanced carrier mobilities, in agreement with the enhanced dynamic mobility observed in the photo-CELIV tests. These results indicate that while both TPP and TPP-OEG effectively passivate oxygen vacancy defects on the SnO_2 surface and suppress charge recombination, the introduction of polar OEG side chains further improves the interfacial compatibility with the active layer and, by modulating film formation kinetics, improves overall active layer morphology and, thereby, enhances photovoltaic performance.

We compared the stability of the inverted devices with the three different ETLs under various conditions (Fig. 6a). After approximately 1000 h of dark storage at room temperature, the SnO_2 and SnO_2/TPP devices retained 91.8% and 95.9% of the initial PCEs, respectively, whereas the SnO_2/TPP-OEG device retained 98.6% of its initial value. Under continuous thermal aging at 85 °C for 288 h, the bare SnO_2 device exhibited rapid PCE degradation, dropping to 45.3% of its initial value, and the SnO_2/TPP device decreased to 85.7%, whereas the SnO_2/TPP-OEG device retained 91.1% of its initial PCE. The enhanced thermal stability of the TPP-OEG devices can be attributed to the defect passivation of SnO_2 and the bridging role of OEG side chains, which improves ETL-active layer coupling and stabilizes the active layer morphology. Finally, device stability under continuous illumination was examined for 120 h (Fig. S19). The device with bare SnO_2 exhibits a rapid decline in performance, retaining only 72.3% of its initial PCE. In contrast, the SnO_2/TPP and SnO_2/TPP-OEG based devices retain 90.3% and 95.6% of their initial PCE, respectively, demonstrating improved operational stability upon interfacial modification.

Furthermore, we investigated the universality of SnO_2/TPP-OEG modification in other active layer systems, including all-small-molecule (BTR-Cl:L8-BO), all-polymer (PM6:PY-IT) and a ternary system (PM6:L8-BO:BTP-eC9), as depicted in Fig. 6c, S20–S22 and Table S4. Both the SnO_2/TPP-OEG devices exhibit higher PCEs than SnO_2/TPP and SnO_2 devices. Notably, the SnO_2/TPP-OEG devices based on the PM6:L8-BO:BTP-eC9 system with DIO as the solvent additive, which suppresses nonradiative recombination by improving molecular ordering and phase separation, achieved a remarkable PCE of 19.60%, representing the highest reported efficiency for inverted OSCs based on SnO_2-ETLs. To the best of our knowledge, this is the highest efficiency for single-junction inverted OSCs to date, as summarized in Fig. 6d and Table S5.

Conclusions

In summary, oligo ethylene glycol tailored porphyrin modification of the SnO_2 electron transport layer is shown to markedly enhance the efficiency and stability of inverted organic solar cells. TPP-OEG simultaneously passivates the surface defects on SnO_2 through strong interactions and regulates the compatibility with the active layer by acting as a molecular bridge between SnO_2 and the active layer. These effects collectively improve the charge extraction, suppress recombination, and enable favorable active layer morphology, thereby enhancing

the efficiency and stability. Notably, a record PCE of 19.60% is achieved in the PM6:L8-BO:BTP-eC9 system for inverted organic solar cells. Our results demonstrate that tailored molecular interface engineering is an effective strategy to improve the efficiencies and stability of OSCs.

Author contributions

J. Wu and X. Peng conceived the idea. L. Meng carried out the synthesis work. J. Wu and Y. Li performed experiments. X. Wang and J. Chen provided the device platform. F. Tang carried out theoretical calculations and the corresponding analysis. T. Wang and B. Fan performed *in situ* UV experiments and analysis. Y. Fu and X. Lu completed the GIWAXS measurements and analysis. J. Wu and Y. Li wrote the original manuscript. Y. Guo helped in the study of device data. X. Peng supervised the project and contributed to the revision of the manuscript.

Conflicts of interest

The authors declare no conflicts of interest.

Data availability

The data that support the findings of this study are available within the article and its supplementary information (SI). Supplementary information: materials and methods, synthesis details, supplementary figures, and supplementary tables. See DOI: https://doi.org/10.1039/d5el00215j.

Acknowledgements

References

1 C. Li, Y. Cai, P. Hu, T. Liu, L. Zhu, R. Zeng, F. Han, M. Zhang, M. Zhang, J. Lv, Y. Ma, D. Han, M. Zhang, Q. Lin, J. Xu, N. Yu, J. Qiao, J. Wang, X. Zhang, J. Xia, Z. Tang, L. Ye, X. Li, Z. Xu, X. Hao, Q. Peng, F. Liu, L. Guo and H. Huang, *Nat. Mater.*, 2025, **24**, 1626–1634.

2 L. Zhu, M. Zhang, G. Zhou, Z. Wang, W. Zhong, J. Zhuang, Z. Zhou, X. Gao, L. Kan, B. Hao, F. Han, R. Zeng, X. Xue, S. Xu, H. Jing, B. Xiao, H. Zhu, Y. Zhang and F. Liu, *Joule*, 2024, **8**, 3153–3168.

3 X. Wang, J. Wu, S. Zhao, M. Chen, T. Shi, X. Xie, Q. Bai, J. Xie, L. Zhang, D. Ma and J. Chen, *Joule*, 2025, **9**, 102135.

4 K. Hu, Y. Ge, H. Yang, Y. Xu, J. Qian, X. Zhu, Y. Wu, C. Cui and Y. Li, *Energy Environ. Sci.*, 2025, **18**, 9194–9204.

5 J. Yuan, Y. Zhang, L. Zhou, G. Zhang, H.-L. Yip, T.-K. Lau, X. Lu, C. Zhu, H. Peng, P. A. Johnson, M. Leclerc, Y. Cao, J. Ulanski, Y. Li and Y. Zou, *Joule*, 2019, **3**, 1140–1151.

6 L. Zhang, Y. Wang, J. Wen, Y. Huang, J. Gao, Y. Duan, S. Park, W. Shin, Z. Ma, M. Liu, S. W. Cho, Y. Park, Y. M. Jung, H. Lee, W. Liu and Y. Liu, *Angew. Chem., Int. Ed.*, 2024, **63**, e202408960.

7 S. S. Shin, S. J. Lee and S. I. Seok, *Adv. Funct. Mater.*, 2019, **29**, 1900455.

8 F. H. Isikgor, S. Zhumagali, L. V. T. Merino, M. De Bastiani, I. McCulloch and S. De Wolf, *Nat. Rev. Mater*, 2023, **8**, 89–108.

9 H. Li and S. Liu, *J. Mater. Chem. A*, 2024, **12**, 9929–9932.

10 Y. Zhao, T. Heumueller, J. Zhang, J. Luo, O. Kasian, S. Langner, C. Kupfer, B. Liu, Y. Zhong, J. Elia, A. Osvet, J. Wu, C. Liu, Z. Wan, C. Jia, N. Li, J. Hauch and C. J. Brabec, *Nat. Energy*, 2022, **7**, 144–152.

11 S. A. Ok, B. Jo, S. Somasundaram, H. J. Woo, D. W. Lee, Z. Li, B.-G. Kim, J. H. Kim, Y. J. Song, T. K. Ahn, S. Park and H. J. Park, *Nat. Commun.*, 2018, **9**, 4537.

12 X. Yu, D. Gao, Z. Li, X. Sun, B. Li, Z. Zhu and Z. a. Li, *Angew. Chem., Int. Ed.*, 2023, **62**, e202218752.

13 G. Li, C. W. Chu, V. Shrotriya, J. Huang and Y. Yang, *Appl. Phys. Lett.*, 2006, **88**, 253503.

14 Q. Chen, C. Wang, Y. Li and L. Chen, *J. Am. Chem. Soc.*, 2020, **142**, 18281–18292.

15 Q. Huang, J. Jing, K. Zhang, Y. Chen, A. Song, Z. Liu and F. Huang, *J. Mater. Chem. A*, 2022, **10**, 23973–23981.

16 S. Li, Z. Fu, W. Chen, X. Lu, J. Xiang, J. Zhang, K. Han, J. Yuan and Y. Zou, *ACS Appl. Mater. Interfaces*, 2025, **17**, 35652–35660.

17 L. Nian, W. Zhang, N. Zhu, L. Liu, Z. Xie, H. Wu, F. Würthner and Y. Ma, *J. Am. Chem. Soc.*, 2015, **137**, 6995–6998.

18 B. Zhang, N. Xu, J. Wan, H. Li, J. Xia, J. Zhu, J. Xu, H. Chen, W. Chen, G. Zeng, Y. Li and Y. Li, *Energy Environ. Sci.*, 2025, **18**, 9550–9560.

19 J. Guo, Y. Wu, R. Sun, W. Wang, J. Guo, Q. Wu, X. Tang, C. Sun, Z. Luo, K. Chang, Z. Zhang, J. Yuan, T. Li, W. Tang, E. Zhou, Z. Xiao, L. Ding, Y. Zou, X. Zhan, C. Yang, Z. Li, C. J. Brabec, Y. Li and J. Min, *J. Mater. Chem. A*, 2019, **7**, 25088–25101.

20 B. Zhou, L. Wang, Y. Liu, C. Guo, D. Li, J. Cai, Y. Fu, C. Chen, D. Liu, Y. Zhou, W. Li and T. Wang, *Adv. Funct. Mater.*, 2022, **32**, 2206042.

21 Y. Jiang, L. Sun, F. Jiang, C. Xie, L. Hu, X. Dong, F. Qin, T. Liu, L. Hu, X. Jiang and Y. Zhou, *Mater. Horizons*, 2019, **6**, 1438–1443.

22 Q. Jiang, L. Zhang, H. Wang, X. Yang, J. Meng, H. Liu, Z. Yin, J. Wu, X. Zhang and J. You, *Nat. Energy*, 2016, **2**, 16177.

23 S. Y. Park and K. Zhu, *Adv. Mater.*, 2022, **34**, 2110438.

24 J. Luke, L. Corrêa, J. Rodrigues, J. Martins, M. Daboczi, D. Bagnis and J.-S. Kim, *Adv. Energy Mater.*, 2021, **11**, 2003405.

25 S. Guang, J. Yu, H. Wang, X. Liu, S. Qu, R. Zhu and W. Tang, *J. Energy Chem.*, 2021, **56**, 496–503.

26 Y. Zhang, X. Zhao, X. Han, Y. Li, Z. Zhang, T. Li, J. Xing, X. Zuo and Y. Lin, *Langmuir*, 2021, **37**, 3173–3179.

27 J. P. Correa Baena, L. Steier, W. Tress, M. Saliba, S. Neutzner, T. Matsui, F. Giordano, T. J. Jacobsson, A. R. Srimath Kandada, S. M. Zakeeruddin, A. Petrozza, A. Abate, M. K. Nazeeruddin, M. Grätzel and A. Hagfeldt, *Energy Environ. Sci.*, 2015, **8**, 2928–2934.

28 W. Dong, C. Zhu, C. Bai, Y. Ma, L. Lv, J. Zhao, F. Huang, Y.-B. Cheng and J. Zhong, *Angew. Chem., Int. Ed.*, 2023, **62**, e202302507.

29 G. Ou, Y. Xu, B. Wen, R. Lin, B. Ge, Y. Tang, Y. Liang, C. Yang, K. Huang, D. Zu, R. Yu, W. Chen, J. Li, H. Wu, L.-M. Liu and Y. Li, *Nat. Commun.*, 2018, **9**, 1302.

30 D. Garcia Romero, L. Di Mario, F. Yan, C. M. Ibarra-Barreno, S. Mutalik, L. Protesescu, P. Rudolf and M. A. Loi, *Adv. Funct. Mater.*, 2024, **34**, 2307958.

31 Z. Suo, Z. Xiao, S. Li, J. Liu, Y. Xin, L. Meng, H. Liang, B. Kan, Z. Yao, C. Li, X. Wan and Y. Chen, *Nano Energy*, 2023, **118**, 109032.

32 S. Li, W. Chen, C. Shi, Y. Gong, K. Yang, L. Jiang, X. Lu, H. Xie, J. Yuan and Y. Zou, *Small*, 2024, **20**, 2405743.

33 P. Shen, M. Yao, G. Wang, R. Mi, W. Guo, Y. Bai and L. Shen, *J. Mater. Chem. A*, 2018, **6**, 17401–17408.

34 H. Gao, X. Wei, R. Yu, F.-Y. Cao, Y. Gong, Z. Ma, Y.-J. Cheng, C.-S. Hsu and Z. a. Tan, *Adv. Opt. Mater.*, 2022, **10**, 2102031.

35 V.-H. Tran, S.-K. Kim and S.-H. Lee, *ACS Omega*, 2019, **4**, 19225–19237.

36 L. Zhang, C. Liu, T. Q. Lai, H. D. Huang, X. B. Peng, F. Huang and Y. Cao, *J. Mater. Chem. A*, 2016, **4**, 15156–15161.

37 Z. Fang, L. Wang, X. Mu, B. Chen, Q. Xiong, W. D. Wang, J. Ding, P. Gao, Y. Wu and J. Cao, *J. Am. Chem. Soc.*, 2021, **143**, 18989–18996.

38 G. B. Bodedla, X. Zhu and W.-Y. Wong, *Aggregate*, 2023, **4**, e330.

39 X. J. Pan, J. F. Wu, L. G. Xiao, B. Yap, R. D. Xia and X. B. Peng, *ChemSusChem*, 2021, **14**, 3614–3621.

40 J. P. Macquet, M. M. Millard and T. Theophanides, *J. Am. Chem. Soc.*, 1978, **100**, 4741–4746.

41 S. Chen, P. Liu, Y. Hua, Y. Li, L. Kloo, X. Wang, B. Ong, W.-K. Wong and X. Zhu, *ACS Appl. Mater. Interfaces*, 2017, **9**, 13231–13239.

42 V. Piradi, G. Zhang, T. Li, M. Zhang, Q. Peng, X. Zhan and X. Zhu, *ACS Appl. Mater. Interfaces*, 2020, **12**, 41506–41514.

43 J. Wu, Y. Li, F. Tang, Y. Guo, H. Wu, L. Yuan, G. Liu, Z. He and X. Peng, *Adv. Funct. Mater.*, 2025, **35**, 2504623.

44 F. Neese, *Wiley Interdiscip. Rev. Comput. Mol. Sci.*, 2022, **12**, e1606.

45 Z. M. Jarzebski and J. P. Marton, *J. Electrochem. Soc.*, 1976, **123**, 199C.

46 S. Das and V. Jayaraman, *Prog. Mater. Sci.*, 2014, **66**, 112–255.

47 T. Lu and Q. Chen, *J. Comput. Chem.*, 2022, **43**, 539–555.

48 L. Kong, B. Fan, X. Huang, Q. Li, C. Zhao and A. K. Y. Jen, *Angew. Chem., Int. Ed.*, 2025, **64**, e202514941.

49 R. N. Mozhchil, A. M. Ionov, S. I. Bozhko, V. S. Bozhko, V. D. Rumyantseva, A. L. Trigub and A. P. Menushenkov, *J. Phys. Conf. Ser.*, 2019, **1238**, 012002.

50 F. Tang, J. Wu, Z. Lin, H. Wu and X. Peng, *Appl. Surf. Sci.*, 2023, **635**, 157720.

51 F. Tang, J. Wu, L. Meng, Q. Zhang, J. Lei, X. Peng and C. Qiu, *Chem. Eng. J.*, 2025, **524**, 169712.

52 Y. Li, J. Ding, C. Liang, X. Zhang, J. Zhang, D. S. Jakob, B. Wang, X. Li, H. Zhang, L. Li, Y. Yang, G. Zhang,

X. Zhang, W. Du, X. Liu, Y. Zhang, Y. Zhang, X. Xu, X. Qiu and H. Zhou, *Joule*, 2021, **5**, 3154–3168.

53 K. Jiang, G. Zhang, G. Yang, J. Zhang, Z. Li, T. Ma, H. Hu, W. Ma, H. Ade and H. Yan, *Adv. Energy Mater.*, 2018, **8**, 1701370.

54 S. Li, Z. Xiao, J.-J. Li, Z.-Y. Hu, Y. Yang, B. Kan, D.-S. Guo, X. Wan, Z. Yao, C. Li and Y. Chen, *Sci. China Chem.*, 2023, **66**, 195–201.

55 Z. Shen, G. Lu, X. Tang, Y. Zhang, S. Li, J. Wang, J. Yu, F. Gao, L. Bu, X. Chen, Y. Zhu, H. Pan, L. Meng and G. Lu, *Nat. Commun.*, 2025, **17**, 655.

56 J. D. Servaites, M. A. Ratner and T. J. Marks, *Energy Environ. Sci.*, 2011, **4**, 4410–4422.

57 F. Fabregat-Santiago, G. Garcia-Belmonte, I. Mora-Seró and J. Bisquert, *Phys. Chem. Chem. Phys.*, 2011, **13**, 9083–9118.

58 W. Shockley and H. J. Queisser, *J. Appl. Phys.*, 1961, **32**, 510–519.

59 Y. Qin, N. Balar, Z. Peng, A. Gadisa, I. Angunawela, A. Bagui, S. Kashani, J. Hou and H. Ade, *Joule*, 2021, **5**, 2129–2147.

60 L. Kong, X. Wang, M. Li, Z. Zhang, M. Chen, L. Zhang, L. Ying, D. Ma and J. Chen, *Adv. Energy Mater.*, 2024, **14**, 2402517.